Factors Driving Variability in the Southern Hemisphere Baroclinic Annular Mode

Qi Liu

May 2025

An Honors Thesis for the Honors Bachelor's degree in:

Mathematics and Economics

College of Arts and Sciences

New York University

Faulty Advisor: Professor Olivier Pauluis

Abstract

The Southern Hemisphere Baroclinic Annular Mode (BAM) dominates intraseasonal variability south of 30 °S, yet the physical origin of its pronounced 20–30-day oscillation has remained unclear. This thesis investigates the mechanisms that sustain that periodicity by combining reanalysis diagnostics with a hierarchy of idealised numerical experiments. Spectral analysis of ERA-Interim reveals coherent peaks near 25 days in both upper-tropospheric eddy kinetic energy (EKE) and lower-tropospheric meridional eddy heat flux (EHF), confirming that the BAM signal is not a statistical artifact but a robust dynamical mode of the real atmosphere.

To isolate the essential dynamics, a two-layer quasi-geostrophic channel model is solved with the Dedalus, a numerical PDE solver package. The model incorporates Newtonian relaxation toward an idealised jet, beta-plane planetary vorticity, and bottom-layer Ekman drag. Parameter sweeps in jet amplitude A, jet half-width S and relaxation time-scale T leads to four flow regimes: stable, weakly nonlinear, nonlinear and super-nonlinear. The nonlinear regime—characterised by moderate baroclinic super-criticality—produces self-sustained oscillations in EKE and EHF whose period, amplitude and phase relationship mirror the observed BAM.

Analytic analysis of the model demonstrates that the oscillation arises from a negative feedback loop: growth of baroclinic waves flattens the layer interface, eroding the meridional temperature gradient and hence the instability that fuels the waves; relaxation then restores the gradient, allowing instability to re-intensify and the cycle to repeat.

These results identify BAM variability as a self-sustained coupled oscillation between baroclinic eddies and the mean state, offering a tractable dynamical framework for improving subseasonal forecasts in the extratropical Southern Hemisphere.

Acknowledgements

1   Introduction

The Earth receives solar radiation unevenly, with most of the incoming energy concentrated in the tropics and much less reaching the poles. This is primarily due to the higher solar incidence angle in the tropics, whereas at higher latitudes, sunlight strikes the Earth at a more oblique angle, and a even larger portion of incoming radiation is reflected by surfaces such as snow and ice. In contrast, outgoing longwave radiation is distributed more uniformly. This differential heating creates a meridional temperature gradient, placing the atmosphere in a thermodynamically unstable state. Large-scale atmospheric circulations arise as a natural consequence of this unstable state, working to reduce the temperature gradients through the transport of heat poleward.

In the midlatitudes, this transport is primarily achieved through baroclinic eddies — small-scale disturbances that grow by extracting potential energy from the mean state. These disturbances are manifestations of baroclinic instability, a dynamical mechanism that converts the available potential energy associated with the zonal mean temperature gradient into kinetic energy, thereby sustaining the variability of midlatitude weather systems.

This conversion process is often described in terms of the Lorenz energy cycle. Zonal available potential energy (ZAPE), generated by meridional gradients in heating, is converted into eddy available potential energy (EAPE) via meridional eddy heat fluxes ($\overline{v'T'}$). Vertical eddy heat fluxes then transform EAPE into eddy kinetic energy (EKE), which powers the motion of transient weather systems. These stages are illustrated schematically in Figure 1 [4,5]. EKE, a key indicator of midlatitude storm activity, is defined as:

$$EKE := \frac{1}{2A} \int_\Omega (u')^2 + (v')^2 dxdy \qquad (1.1)$$

where A is the area of the domain Ω and u', v' are velocity anomalies in zonal (east-west) and meridional (north-south) direction, respectively. All the quantities will be defined and explained more rigorously in the later chapters.

This thesis will focus on the variability of eddy fluxes of heat (EFH) and eddy kinetic energy in the extratropical atmosphere of the Southern Hemisphere.

Earth's climate demonstrates several robust periodic variabilities, such as seasonality and tidal waves. Recent studies have identified a robust periodic variability in the Southern Hemisphere that was largely overlooked in the past. Such variability has a baroclinic structure associated with the variability in the Southern Hemisphere baroclinic annular mode (BAM) [3] that dominates the variance in the eddy kinetic energy. The BAM is characterized by fluctuations in the lower tropospheric eddy fluxes of heat and upper tropospheric eddy kinetic energy that span much of the Southern Hemisphere. It is thus associated with
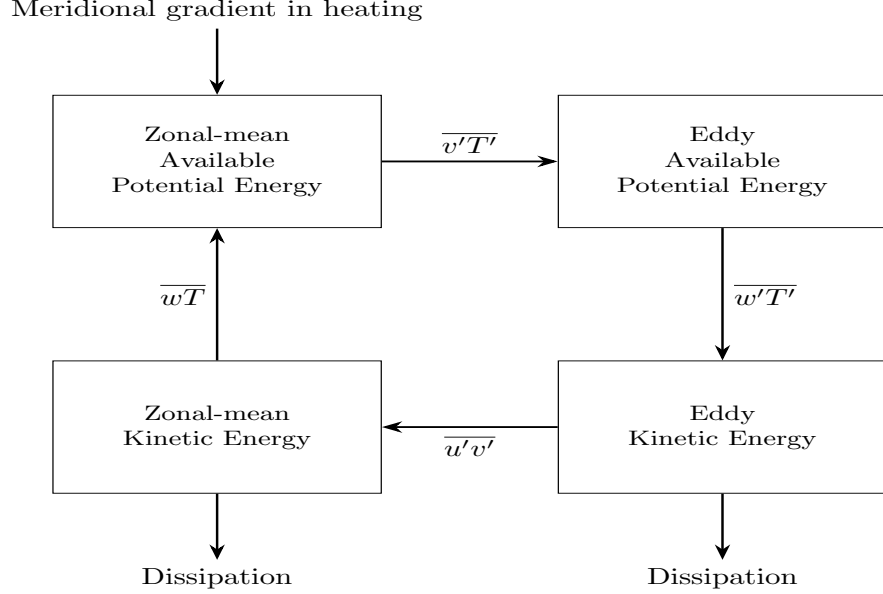
Meridional gradient in heating

| Zonal-mean Available Potential Energy | $\overline{v'T'}$ → | Eddy Available Potential Energy |

$\overline{wT}$ ↑ $\overline{w'T'}$ ↓

| Zonal-mean Kinetic Energy | ← $\overline{u'v'}$ | Eddy Kinetic Energy |

Dissipation   Dissipation

Figure 1: Energy cycling processes in the extratropical atmosphere [4] [5]. $\overline{(\cdot)}$ denotes the zonal mean i.e. $\frac{1}{L}\int(\cdot)dx$ and $(\cdot)'$ denotes the eddy component of the flow, i.e. $(\cdot) - \overline{(\cdot)}$.

variations in both the generation (in the lower troposphere) and amplitude (in the higher troposphere) of wave activity throughout the extratropical Southern Hemisphere.

The evolution of BAM events can be quantified by tracking EKE in the upper troposphere and EFH in the lower troposphere. Using the ERA-Interim reanalysis dataset from the European Centre for Medium-Range Weather Forecasts (ECMWF), a time series analysis (Figure 2) reveals a robust periodicity in BAM-related EKE and EFH on time scales of 20–30 days. This is significantly longer than the typical 3–5 day time scale associated with individual synoptic weather systems. Understanding the dynamics underlying BAM is crucial, as its longer time scale offers potential for extending the predictability of atmospheric variability beyond the traditional weather forecast window. In this study, we investigate the mechanisms that give rise to this periodic variability.

We started with a simplified 2-layer Quasi-geostrophic (QG) model.

2 Two-Layer Barotropic Quasi-Geostrophic Equations Through a Channel

Although the full derivation of the QG equations is quite lengthy and technical, we attempt to give a quick, intuitive derivation here. The full derivation can be found in various geophysical fluid dynamics textbooks such as *Atmospheric and Oceanic Fluid Dynamics* by Vallis [5]. We must start with the full two-layer shallow
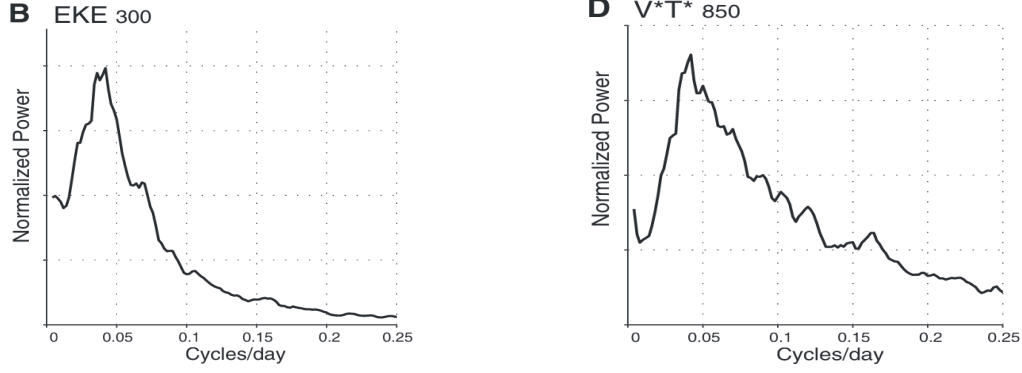
Figure 2: (Left) Spectra of EKE at 300 hPa, (right) Spectra of EFH at 850 hPa

water model. The shallow water equations are a set of fluid equations that describe the horizontal flow of a thin layer of incompressible fluid under the influence of gravity and the Coriolis effect. They are derived by vertically integrating the Navier–Stokes equations under the assumption that the horizontal length scales are much larger than the vertical depth, allowing the hydrostatic approximation to be applied. Let $h(x, y, t)$ denote the fluid thickness and $\vec{u} = (u, v)$ the horizontal velocity field. The conservation of mass (continuity equation) is given by

$$\frac{\partial h}{\partial t} + \nabla \cdot (h\vec{u}) = 0, \tag{2.1}$$

which expresses the local change in fluid depth due to divergence in the horizontal flow. The momentum equations, derived from Newton's second law and assuming hydrostatic balance in the vertical, are

$$\frac{\partial \vec{u}}{\partial t} + \vec{u} \cdot \nabla \vec{u} + f\hat{k} \times \vec{u} = -g\nabla h, \tag{2.2}$$

where f is the Coriolis parameter, g is gravitational acceleration, and $\hat{k}$ is the unit vector in the vertical direction. These equations form the basis for a wide range of studies in atmospheric and oceanic dynamics, capturing phenomena such as gravity waves, geostrophic balance, and Rossby waves. Although simplified, they retain key nonlinear and rotational effects and serve as the starting point for more advanced layered and quasi-geostrophic models.

To further simplify the governing equations while retaining the essential dynamics, the quasi-geostrophic (QG) approximation is applied. This approximation is valid in regimes characterized by small Rossby numbers, typical of large-scale, slow-moving atmospheric motions away from the equator. Under this assumption, the flow is nearly geostrophic, and the governing equations reduce to a balance between advection of potential vorticity and planetary vorticity gradients. In the two-layer QG model, each layer evolves according to its own potential vorticity equation, but the coupling between layers is retained through interfacial displacement,

5

allowing for the representation of baroclinic instability and eddy–mean flow interactions.

The system considered here is a two-layer quasi-geostrophic flow through a zonally periodic channel. The channel represents an idealized midlatitude atmosphere bounded in the meridional direction with vanishing normal gradient (Neumann type) conditions and periodic in the zonal direction. The governing equations (2.3)–(2.7) describe the time evolution of potential vorticity in each layer, q_1 and q_2, subject to planetary vorticity gradients (the β-effect), dissipation (r), and a simple Newtonian relaxation to a prescribed equilibrium state (Q_1, Q_2). The potential vorticity in each layer includes contributions from relative vorticity and interfacial deformation due to stratification, characterized by the deformation wavenumber k_d. The streamfunctions ψ_1 and ψ_2 determine the horizontal velocity fields in each layer via the geostrophic relation. This setup provides a tractable yet powerful model for exploring the dynamics of baroclinic variability and eddy–mean flow interactions in an idealized setting.

$$\frac{\partial q_1}{\partial t} + J(\psi_1, q_1) + \beta v_1 + \frac{1}{T}(\bar{q}_1 - Q_1) = 0 \tag{2.3}$$

$$\frac{\partial q_2}{\partial t} + J(\psi_2, q_2) + \beta v_2 + \frac{1}{T}(\bar{q}_2 - Q_2) + r\nabla^2\psi_2 = 0 \tag{2.4}$$

$$q_1 = \nabla^2\psi_1 - \frac{k_d^2}{2}(\psi_1 - \psi_2) \tag{2.5}$$

$$q_2 = \nabla^2\psi_2 + \frac{k_d^2}{2}(\psi_1 - \psi_2) \tag{2.6}$$

$$\boldsymbol{v_i} = \begin{pmatrix} u_i \\ v_i \end{pmatrix} = \nabla^\perp\psi_i = \begin{pmatrix} -\psi_{iy} \\ \psi_{ix} \end{pmatrix}, \quad i = 1, 2 \tag{2.7}$$

A quick summary is that the two-layer QG model was derived under the setup that there are two layers of fluid flows governed by the primitive equations (momentum equations, hydrostatic balance, mass conservation, and thermodynamic equation) with the simplifying assumption that the Rossby number of the flows is small, so the flow is in quasi-geostrophic balance.

Subscript $i = 1, 2$ corresponds to the top and bottom layer, respectively. In Equation 2.3 and Equation 2.4, q_i is the potential vorticity, a materially conserved quantity, of each layer. ψ_i is the stream-function with contour lines tracing out the flow line of the velocity field (u_i, v_i). An important remark is that $(\psi_1 - \psi_2)$ is also a measure of the vertical displacement of the layers' interface. In other words, ψ_i is a measure of the thickness of each layer. $r\nabla^2\psi_2$ parametrizes the Ekman drag of the bottom layer due to friction at the lower boundary. β controls the beta effect due to the variation of the Coriolis parameter with latitude and $\frac{k_d^2}{2} = (\frac{2f_0}{NH})^2$, with boundary conditions of the Neumann type on the north and south walls.

Equation 2.3–7 conserves the total energy, defined as the sum of kinetic energy in each layer and the available potential energy due to interfacial displacement:

$$E := \frac{1}{2}|\nabla\psi_1|^2 + \frac{1}{2}|\nabla\psi_2|^2 + \frac{k_d^2}{4}(\psi_1 - \psi_2)^2.$$

A detailed derivation of the conservation law for this energy is provided in Appendix A, where the equations are cast into energy form. Specifically, we have:

$$\frac{d}{dt}\int_\Omega \left[\frac{1}{2}|\nabla\psi_1|^2 + \frac{1}{2}|\nabla\psi_2|^2 + \frac{k_d^2}{4}(\psi_1 - \psi_2)^2\right] = \int_\Omega \left(\psi_1\frac{\bar{q}_1 - \bar{Q}_1}{T} + \psi_2\frac{\bar{q}_2 - \bar{Q}_2}{T}\right), \tag{2.8}$$

where the right-hand side represents the diabatic and frictional sources or sinks of energy.

To better understand the energetics, we now separate the contributions from the mean flow and the eddies. This decomposition underpins the interpretation presented in Figure 1, and it begins with the zonal-mean quasigeostrophic potential vorticity equations:

$$\frac{\partial\bar{q}_1}{\partial t} = -\frac{\partial}{\partial y}\overline{v_1' q_1'} - \frac{\bar{q}_1 - \bar{Q}_1}{T}, \tag{2.9}$$

$$\frac{\partial\bar{q}_2}{\partial t} = -\frac{\partial}{\partial y}\overline{v_2' q_2'} - \frac{\bar{q}_2 - \bar{Q}_2}{T} + r\left(\frac{\partial\overline{u}_2}{\partial y}\right), \tag{2.10}$$

where perturbations are defined by $(\cdot)' = (\cdot) - \overline{(\cdot)}$, i.e., deviations from the zonal mean.

To derive the zonal energy balance, we multiply (2.9) by $-\overline{\psi}_1$ and (2.10) by $-\overline{\psi}_2$, integrate over the domain, and sum the resulting expressions. This yields the flux form of the evolution equations for the zonal mean kinetic energy and zonal available potential energy, capturing the interactions between mean and eddy fields.

$$\frac{d}{dt}\int_\Omega [\frac{1}{2}|\nabla\overline{\psi_1}|^2 + \frac{1}{2}|\nabla\overline{\psi_1}|^2 + \frac{k_d^2}{4}(\overline{\psi_1} - \overline{\psi_2})^2] = \int_\Omega \overline{\psi_1}\frac{\bar{q}_1 - \bar{Q}_1}{T} + \overline{\psi_2}\frac{\bar{q}_2 - \bar{Q}_2}{T} \tag{2.11}$$

$$-\int_\Omega \psi_1'\frac{\partial\overline{\psi_1}}{\partial y}\frac{\partial q_1'}{\partial x} + \psi_2'\frac{\partial\overline{\psi_2}}{\partial y}\frac{\partial q_2'}{\partial x} \tag{2.12}$$

Then to arrive at an expression for EKE, subtract (2.3) and (2.4) by (2.9) and (2.10) respectively and integrate over the domain, then summing them up, we get:

$$\frac{d}{dt}\int_\Omega [\frac{1}{2}|\nabla\psi_1'|^2 + \frac{1}{2}|\nabla\psi_2'|^2 + \frac{k_d^2}{4}(\psi_1' - \psi_2')^2] = \int_\Omega \psi_1'\frac{\partial\overline{\psi_1}}{\partial y}\frac{\partial q_1'}{\partial x} + \psi_2'\frac{\partial\overline{\psi_2}}{\partial y}\frac{\partial q_2'}{\partial x} \tag{2.13}$$

7

Equation (2.11) describes the conservation law for EKE defined as the kinetic energy of the "variance flow" after a mean-variance decomposition, i.e.:

$$EKE_i := \int_\Omega \frac{1}{2} |\nabla \psi_i'|^2 \tag{2.14}$$

We can then identify one of the two key periodic quantities in BAM in our QG model. We can also identify eddy heat flux $\overline{v'T'}$, the other periodic quantity in BAM as $\overline{v'(\psi_1 - \psi_2)'}$. We argue such equivalence by thinking about ψ_1 and ψ_2 not only as the stream function but also as a measure of the thickness of each layer.(Details in Appendix A) And if we assume that the top layer is composed of cold air and the bottom layer is composed to warm air, then the difference is exactly a measure of temperature, thus we define:

$$EHF_i := \int_\Omega (v_i')(\psi_1 - \psi_2)' \tag{2.15}$$

We expect BAM-associated variation to be present in the 2 quantities above in our 2-layer channel QG model by the following hypothesis:

If the flow is baroclinically unstable, baroclinic instability flattens the layer interface, leading to a decrease in thickness and temperature gradient. A flattened layer interface weakens baroclinic instability, allowing the profile to restore to the relaxation profile. Then the flow becomes more baroclinically unstable again due to increasing thickness and temperature gradient. This negative feedback loop generates the periodic behavior of EKE and EHF. We will first confirm such a hypothesis through a numerical simulation and explore the parameter regimes where such a feedback loop is sustainable.

3   Numerical Simulation Setup

The two-layer quasi-geostrophic system we're studying resembles the full Navier–Stokes equations, which are famously difficult to solve in general. In fact, proving whether smooth solutions to the three-dimensional Navier–Stokes equations always exist is one of the Millennium Prize Problems. Our QG model is a simplified, layered version of this system, but it still retains many of the core nonlinearities, especially through the Jacobian advection terms and the coupling between layers due to interfacial deformation. On top of that, spatially varying forcing, dissipation, and relaxation terms make the system analytically intractable. For these reasons, we turn to numerical simulations as the only viable approach to understand how energy and heat evolve in this system, and to test our hypothesis about the self-sustained oscillations in eddy kinetic energy (EKE) and eddy heat flux (EHF).

To solve the two-layer QG system numerically, we use the `Dedalus` Python package, a highly flexible spec-

tral framework for solving partial differential equations (PDEs). Dedalus supports the solution of general integral-differential equations with arbitrary boundary conditions using spectral methods. It is particularly well suited for geophysical fluid dynamics problems because it handles complex boundary conditions, nonlinear terms, and time-dependent forcing naturally. By leveraging Fourier and Chebyshev basis functions, Dedalus achieves high numerical accuracy and efficiency, especially for problems defined in periodic and bounded domains. This makes it an ideal tool for simulating the QG equations in a zonally periodic, meridionally bounded channel with Neumann boundary conditions.

In our numerical implementation, we evolve the potential vorticity fields q_1 and q_2, since they are the prognostic variables in the quasi-geostrophic equations. The time evolution equations for q_i are explicitly given in Equations (2.3) and (2.4), with nonlinear advection, planetary vorticity gradients, relaxation, and dissipation terms. However, because q_i and ψ_i are linked through a diagnostic elliptic relationship (Equations (2.5) and (2.6)), the streamfunctions must be recovered from the potential vorticities at each time step by solving a Helmholtz-type equation. The velocity fields are then derived from ψ_i via the geostrophic relation $\vec{v}_i = \nabla^\perp \psi_i$, and are used to compute the nonlinear Jacobian terms $J(\psi_i, q_i)$. We use the `classRK443` timestepper from the Dedalus library, which implements a third-order, four-stage implicit-explicit (IMEX) Runge–Kutta scheme [1]. This scheme treats the linear stiff terms implicitly and the nonlinear terms explicitly, offering a stable and efficient approach for evolving the system. The domain is discretized spectrally, using Fourier modes in the zonal (periodic) direction and Chebyshev polynomials in the meridional direction to enforce Neumann boundary conditions at the channel walls. Nonlinear products are computed in physical space and dealiased to prevent aliasing errors.

There are multiple input parameters in our model, some of which are intrinsic to the two-layer quasi-geostrophic (2LQG) equations, while others arise from the numerical discretization. For the 2LQG model parameters, we fix $\beta = 0.05$ and $k_d = 1$, and we parameterize the bottom-layer Ekman drag coefficient r following classical Ekman layer theory [2]. Specifically, we set

$$r = 0.16 \left(\frac{U}{\lambda} \right), \quad \text{where} \quad \lambda = \frac{L}{50 \cdot 2\pi}.$$

Here, L denotes the horizontal length scale. For the numerical setup, we fix the domain size to $L_x = 60$ and $L_y = 30$, and discretize it using $N_x = 512$ and $N_y = 256$ grid points in the x and y directions, respectively.

We prescribe the relaxation profiles Q_1 and Q_2 appearing in equations (2.3) and (2.4) using the following

antisymmetric functions:

$$Q_1(y) = 2A\left[\left(S^2 + \frac{1}{2}\right)\tanh(Sy) - S^2\tanh^3(Sy)\right],$$

$$Q_2(y) = -2A\left[\left(S^2 + \frac{1}{2}\right)\tanh(Sy) - S^2\tanh^3(Sy)\right],$$

where A controls the amplitude and S the width of the meridional gradient.

One can verify that $\psi_1 = -A\tanh(Sy)$ and $\psi_2 = A\tanh(Sy)$ are solutions to (3.3) and (3.4) with Q_1 and Q_2 as the potential vorticity profile. Consequently, S controls the width of the zonal jet in the y direction. A controls the magnitude of the zonal jet. As mentioned above, ψ_2 is also a measure of the thickness of the bottom layer. So ψ_2 is the layer interface where S controls the slope of the profile around $y = 0$, and A controls the amplitude of the profile. In addition, T controls the relaxation time scale. Figure 3 provides an example of a visualization of a specific relaxation profile.
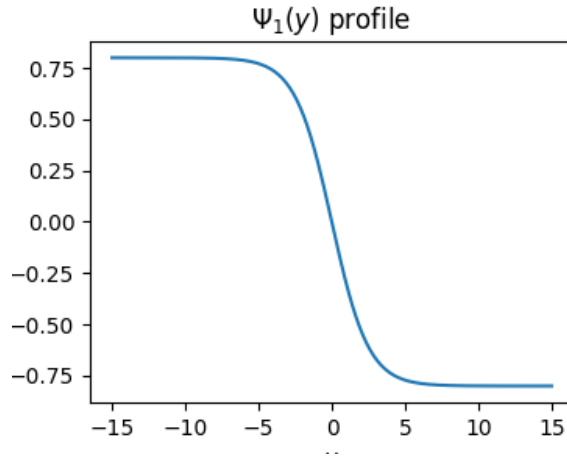

Figure 3: Q_1's corresponding ψ_1 profile with A $= 0.8$, S $= 0.4$

We keep these three parameters (A, S, T) tunable and explore different parameter regimes.

As noted above, it is important that our flow is baroclinically unstable. The Charney–Stern–Pedlosky (CSP) necessary condition [5] for baroclinic instability, one of the well-known necessary conditions, states that q_{1y} changes sign in the interior of the fluid for an unbounded domain. It is not a sufficient condition. And since our model has boundary conditions on the north-south wall, the baroclinic instability criteria are more sensitive to the inputs. In general, a larger value for S, which is equivalent to having a narrower zonal jet, requires higher values of A for the flow to be unstable. This combination produces a very strong and narrow zonal jet, which is not physically realistic in the context of Earth's dynamics. So we restrict our attention to the case where S is small.
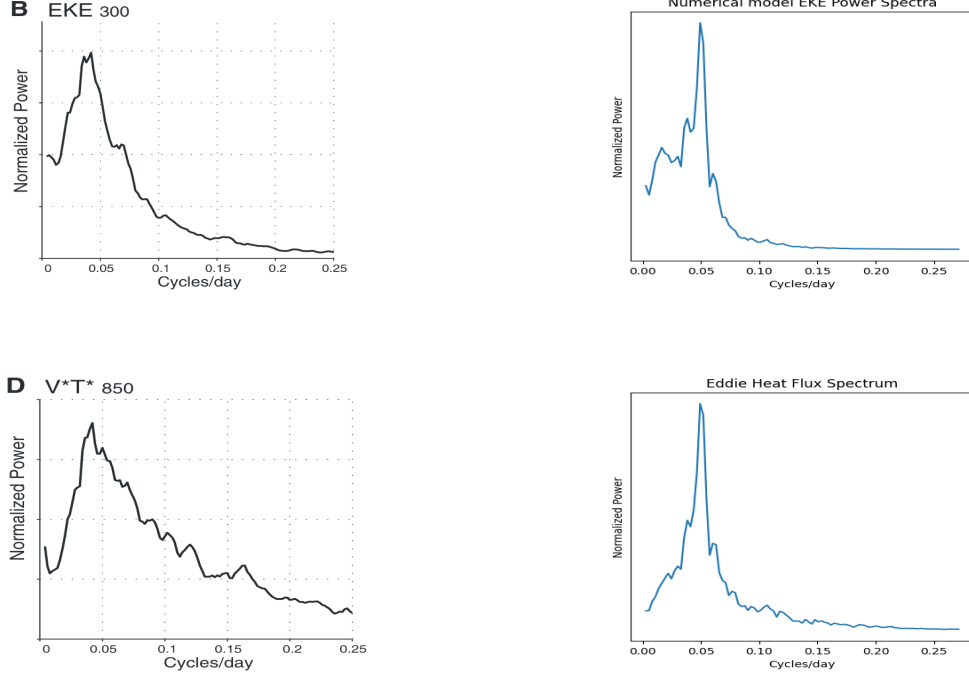
Figure 4: The left panel is the same as Figure 1. The right panel shows the power spectra in the numerical simulation. The spectra are generated through spectral analysis. We spin up the model from some random perturbation as an initial condition until it reaches a dynamically balanced state. Then we let the model roll out for a few years and record the EKE and EFH. After we obtain the time series data of both quantities, we divide them into pieces with time span of 365 days. For each piece, we performed a discrete Fourier transform on each piece and averaged over all pieces. The spectra correspond to the magnitude of the fourier coefficient at each frequency.

Since our model is non-dimensional, translating the simulation results to real-world interpretations requires dimensionalization. However, because our primary focus is on the periodicity of the BAM-associated oscillations, it is sufficient to dimensionalize only the time variable, i.e., determine the real-world time scale corresponding to t = 1 in our model. A natural selection of time scale arises from the Ekman drag parametrization. The parameters U and L that are used in the parametrization gives the natural time scale: $t = \frac{L}{U}$. Together with the usual scaling of atmospheric flows: $U \sim \mathcal{O}(10m/s)$, $L \sim \mathcal{O}(1000km)$, we have $t \sim \mathcal{O}(10^4 s)$ which is about 0.1 day.

4   Results

We first validate our hypothesis by demonstrating that certain parameters reproduce the highly similar variability in EKE and EFH as the observational data. Both EKE and EFH exhibit a frequency peak around 20 days per cycle (Figure 3). The parameter choices of this numerical simulation are given in Table 1 and a movie of this simulation will be provided in the Appendix:

A	S	r	β	T	k_d	x	y
0.4	0.6	0.025	0.05	2	1	$\in [0, 60]$	$\in [-15, 15]$

Table 1: parameter summary

We then explore how each parameter influences the periodic behavior of EKE and EHF. Figure 4 provides an ensemble of EKE spectra ranging different parameters. Based on their baroclinic supercriticality, we categorize the dynamics into 4 different regimes: stable, weakly non-linear, non-linear, super non-linear.
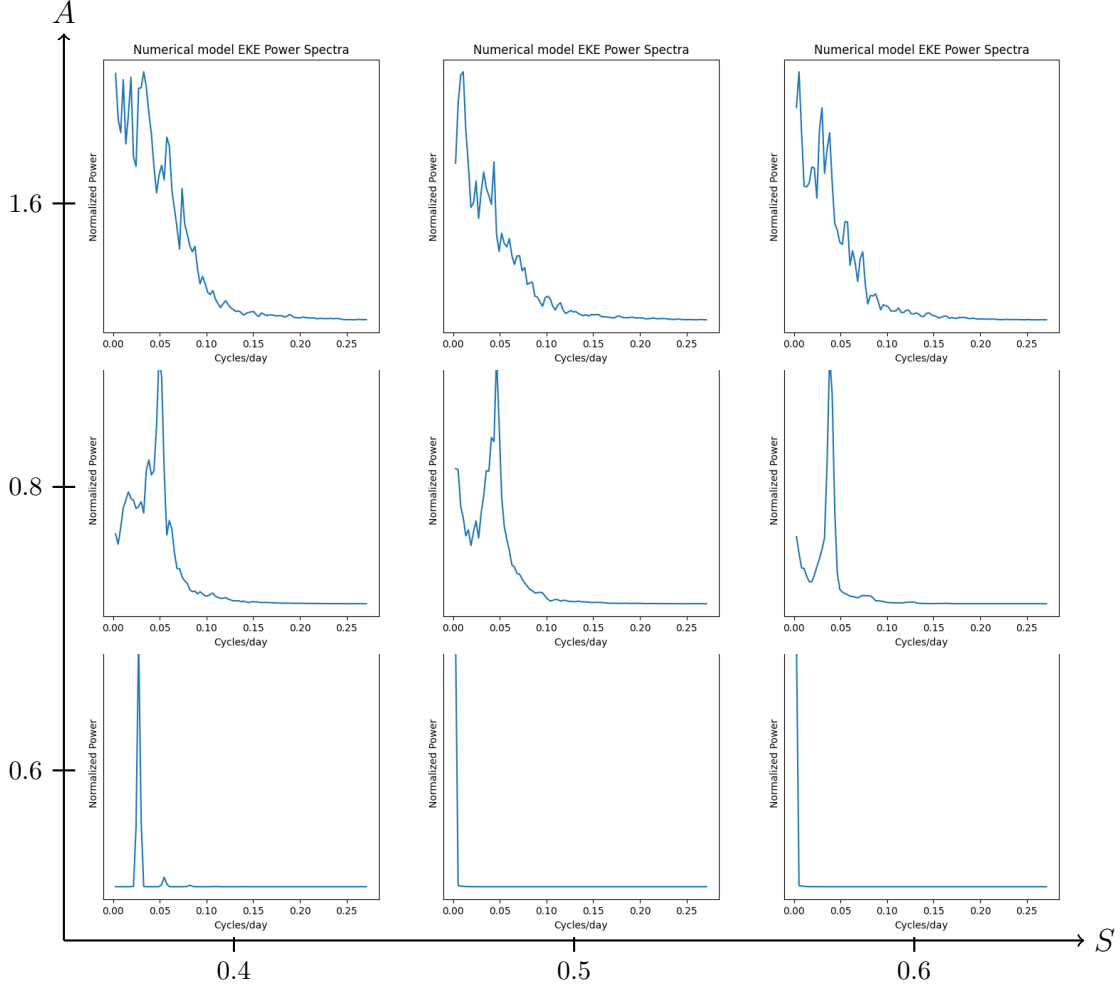

Figure 5: EKE spectra for different values of A and S

Unfortunately, the usual baroclinic supercriticality index $\xi = \frac{U}{\beta}$ [2] cannot be applied here since our fluid is flowing in a confined domain and traditional analysis assumes no boundary condition. We cannot provide an universal indicator to separate the 4 dynamics. However, we identified that the magnitude of EKE fluctuation turns out to be a solid indicator for this numerical model. We now summarize the periodic behavior of EKE in each regime:

- Stable flow ($\leq 1\%$ EKE fluctuation):

  Stable flows correspond to the parameter regime of high S, low A, or small T. In these scenarios, the baroclinic instability criterion are not satisfied so the flow cannot develop eddies that arise from baroclinic instability. The velocity profile of the flow agrees with the relaxation profile. So the flow does not exhibit any periodicity in both EKE and EFH. The plot at (0.6,0.6) in Figure 4 is an example of the EKE spectrum for flow in this regime.

- Weakly non-linear flow ($\leq 1\% \leq 5\%$ EKE fluctuation)

  Weakly non-linear flows correspond to the parameter regime where the baroclinic instability criterion is marginally satisfied. The flow develops baroclinic instability that are not strong enough for the non linear behavior of the QG equations to dominate. In the weakly non-linear regime, EKE demonstrates a very dominant oscillation of a single frequency. Plot at (0.6,0.8) is an example of flow in this regime. EFH and EKE has matching peak frequency.

- Non-linear flow ($\leq 5\% \leq 50\%$ EKE fluctuation).

  Non-linear flows correspond to the parameter regime where the baroclinic instability criterion is satisfied but not greatly exceeded. This regime enables the negative feedback loop between the thickness gradient and baroclinic instability. Plots at (0.4,0.8) in Figure 4 and Figture 5 are the EKE and EFH spectra of flows in this regime.

- Super non-linear flow ($\geq 50\%$ EKE fluctuation)

  Super non-linear flow correspond to the parameter regime of low S, high A, or large T. Stronger instability causes peak frequency to shift to lower frequency in EKE and to higher frequency in EFH. Flows in this regime also demonstrates less defined frequency peak, especially in EFH.
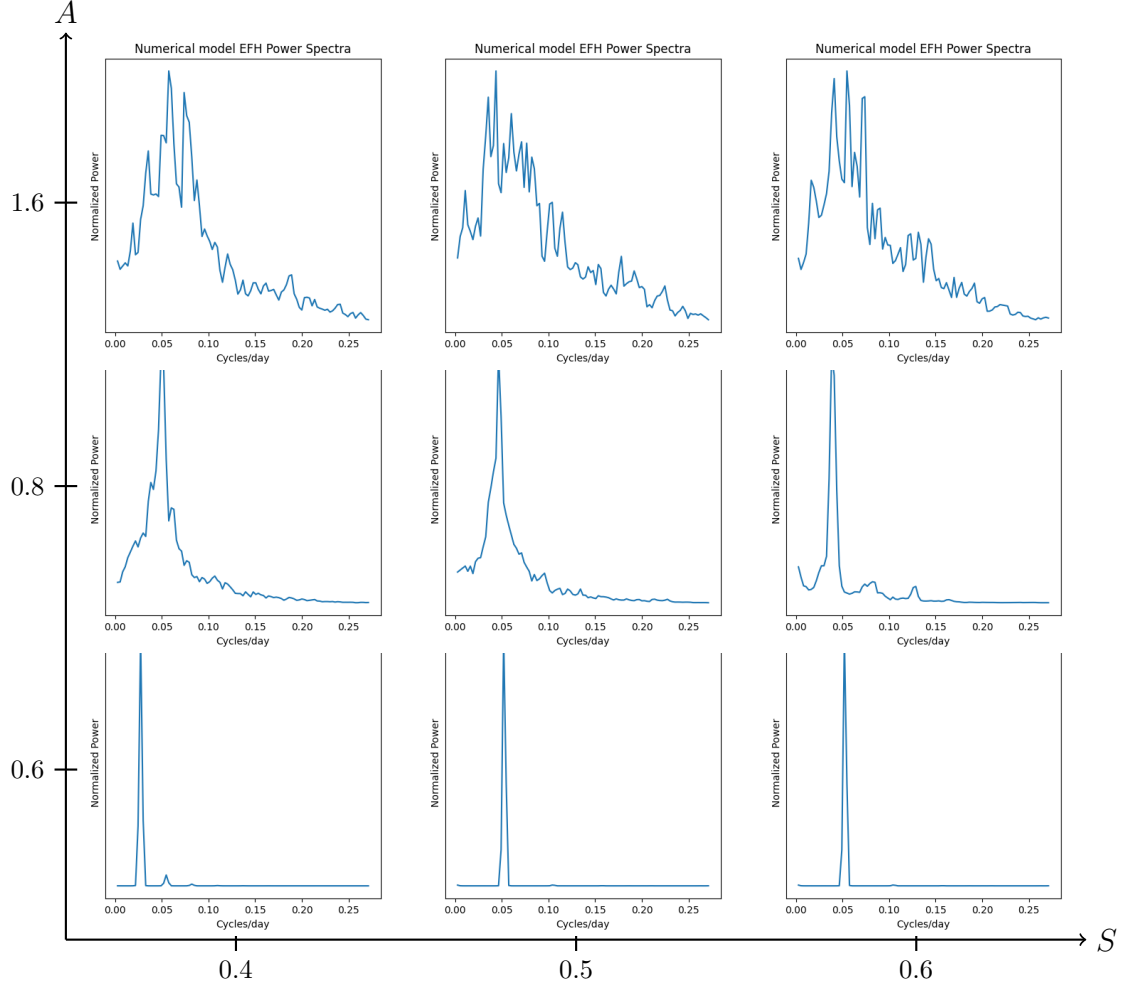
Figure 6: EFH spectra for different values of A and S

Appendix A

We first derive (Equation 2.8):

$$\frac{d}{dt}\int_\Omega\left[\frac{1}{2}|\nabla\psi_1|^2+\frac{1}{2}|\nabla\psi_2|^2+\frac{k_d^2}{4}(\psi_1-\psi_2)^2\right]=\int_\Omega\left(\psi_1\frac{\bar{q}_1-\bar{Q}_1}{T}+\psi_2\frac{\bar{q}_2-\bar{Q}_2}{T}\right) \tag{.1}$$

We start with Equation (3.1) and Equation (3.2), with Equation (3.3) and Equation (3.4) sub in

$$\frac{D}{Dt}\left[\nabla^2\psi_1-\frac{1}{2}k_d^2(\psi_1-\psi_2)\right]+\beta\frac{\partial\psi_1}{\partial x}=-\frac{1}{T}(\bar{q}_1-Q_1),$$

$$\frac{D}{Dt}\left[\nabla^2\psi_2+\frac{1}{2}k_d^2(\psi_1-\psi_2)\right]+\beta\frac{\partial\psi_2}{\partial x}=-\frac{1}{T}(\bar{q}_2-Q_2),$$

14

where $k_d^2/2 = (2f_0/NH)^2$. On multiplying these two equations by $-\psi_1$ and $-\psi_2$, respectively, and integrating over the horizontal domain, the advective term in the material derivatives and the beta term all vanish, and we obtain

$$\int_\Omega \left[\frac{d}{dt}\frac{1}{2}(\nabla\psi_1)^2 + \frac{1}{2}k_d^2\psi_1\frac{d}{dt}(\psi_1 - \psi_2) \right] dA = \int_\Omega \left(\psi_1\frac{\bar{q}_1 - \bar{Q}_1}{T} \right),$$

$$\int_\Omega \left[\frac{d}{dt}\frac{1}{2}(\nabla\psi_2)^2 - \frac{1}{2}k_d^2\psi_2\frac{d}{dt}(\psi_1 - \psi_2) \right] dA = \int_\Omega \left(\psi_2\frac{\bar{q}_2 - \bar{Q}_2}{T} \right).$$

Adding these gives

$$\frac{d}{dt}\int_A \left[\frac{1}{2}(\nabla\psi_1)^2 + \frac{1}{2}(\nabla\psi_2)^2 + \frac{k_d^2}{4}(\psi_1 - \psi_2)^2 \right] dA = \int_\Omega \left(\psi_1\frac{\bar{q}_1 - \bar{Q}_1}{T} + \psi_2\frac{\bar{q}_2 - \bar{Q}_2}{T} \right).$$

This is the energy conservation statement for the two-layer channeled QG model.

Now we provide the movies of the simulation with peak oscillations that most mirror the observational frequency with parameters described in Table 1.

You can access the videos at: Movie of evolution of q_i and $\Delta\psi_i$, the potential vorticity and relative vorticity, respectively. And at: evolution of EKE in the top layer.

References

[1] Uri M. Ascher, Steven J. Ruuth, and Raymond J. Spiteri. Implicit-explicit runge–kutta methods for time-dependent partial differential equations. *Applied Numerical Mathematics*, 25(2-3):151–167, 1997.

[2] Isaac M. Held and Vitaly D. Larichev. A Scaling Theory for Horizontally Homogeneous, Baroclinically Unstable Flow on a Beta Plane. *Journal of the Atmospheric Sciences*, April 1996. Section: Journal of the Atmospheric Sciences.

[3] David W. J. Thompson and Elizabeth A. Barnes. Periodic Variability in the Large-Scale Southern Hemisphere Atmospheric Circulation. *Science*, 343(6171):641–645, February 2014. Publisher: American Association for the Advancement of Science.

[4] David W. J. Thompson and Jonathan D. Woodworth. Barotropic and Baroclinic Annular Variability in the Southern Hemisphere. *Journal of the Atmospheric Sciences*, 71(4):1480–1493, April 2014.

[5] Geoffrey K. Vallis. *Atmospheric and Oceanic Fluid Dynamics: Fundamentals and Large-Scale Circulation.* Cambridge University Press, 2 edition, 2017.